Available online at www.sciencedirect.com
SCIENCE DIRECT®
Journal of Sound and Vibration 274 (2004) 821–841
JOURNAL OF SOUND AND VIBRATION
www.elsevier.com/locate/jsvi

Vibration analysis of a flexible rotating disk with angular misalignment

Jin Wook Heo, Jintai Chung*

Department of Mechanical Engineering, Hanyang University, 1271 Sa-1-dong, Ansan, Kyunggi-do 425-791, Republic of Korea

Received 21 November 2002; accepted 23 May 2003

Abstract

The dynamic characteristics and responses of a flexible rotating disk are analyzed, when the disk has angular misalignment that is defined by the angle between the rotation and symmetry axes. Based on the von Karman strain theory and the Kirchhoff plate theory, three equations of motion are derived for the transverse, radial and tangential displacements when the disk has angular misalignment. The derived equations are fully coupled partial differential equations through the transverse, radial and tangential displacements. In particular, the equation of transverse motion is non-linear while the others are linear. After these partial differential equations and the associated boundary conditions are transformed into a weak form, the weak form is discretized to a non-linear matrix–vector equation by using the finite element method. The non-linear equation is linearized in the neighbourhood of a dynamic equilibrium position, and then the natural frequencies and mode shapes are computed. In addition, the dynamic time responses are obtained by applying the generalized-α method. The effects of angular misalignment on the natural frequencies, the mode shapes and the dynamic responses are investigated. The analysis shows that the angular misalignment causes the natural frequency split and the out-of-plane mode with only one nodal diameter and no nodal circle has the largest frequency split. It is also found that the angular misalignment yields the amplitude modulations in the transverse, radial and tangential dynamic responses.

1. Introduction

Rotating disks have been interesting research topics for decades because the disks have various applications, for example, circular saws, disk brakes, fly wheels, turbine rotors and data storage disks. A lot of studies on the rotating disks have been reported. Some of them have been devoted

*Corresponding author. Tel.: +82-31-400-5287; fax: +82-31-406-5550.
E-mail address: jchung@hanyang.ac.kr (J. Chung).

0022-460X/03/$ - see front matter
doi:10.1016/S0022-460X(03)00573-X

to the dynamics of asymmetric or imperfect circular disks. Tobias and Arnold [1] studied the influence of imperfection on the backward and forward travelling wave of a rotating disk experimentally. Leissa et al. [2] investigated the vibration of a circular plate with non-uniform edge constraints. Perturbation solutions to determine the natural frequencies of almost annular or circular disks were presented by Parker and Mote [3]. They also analyzed the free vibration of coupled, asymmetric disk–spindle systems in which both the disk and spindle are flexible [4]. Tseng and Wickert [5,6] studied bolted and eccentrically clamped annular plates. The transverse free and forced vibrations of a rectangularly orthotropic rotating disk were analyzed by Phylactopoulos and Adams [7,8]. Related to Refs. [5,6], the spatial modulation of repeated vibration modes in rotationally periodic structures are studied by Kim et al. [9]. Recently, Chung and his co-worker [10,11] studied the effects of misalignment between the axes of symmetry and rotation on the natural frequencies and mode shapes of a rotating disk. They treated a rotating disk with only translational misalignment, in which the axes of symmetry and rotation are parallel but not aligned. However, a real rotating disk may have a different type of misalignment called the angular misalignment. The angular misalignment is defined by the angle between the axes of symmetry and rotation when these axes are not parallel. To the authors' knowledge, the effects of angular misalignment on the dynamic characteristics and responses of a rotating disk have not been analyzed yet.

The dynamic characteristics of a rotating disk with angular misalignment are investigated in this paper. Using Hamilton's principle based on the Kirchhoff plate theory and von Karman strain theory, the equations of the radial, tangential and transverse motions are derived when a flexible disk rotates with angular misalignment. The finite element method is used to obtain approximate solutions. The weak form is derived from the equations of motion and the associate boundary conditions and then a non-linear matrix–vector equation is obtained by discretization of the weak form with the four-node annular sector elements defined in Ref. [11]. After the matrix–vector equation is linearized around a dynamic equilibrium position, the effects of angular misalignment on the natural frequencies and mode shapes are analyzed. Furthermore, in order to compute dynamic responses from the non-linear equation, the generalized-α time integration method [12] is applied to the equation along with the Newton–Raphson method. The effects of angular misalignment on the dynamic responses are also analyzed from the computed responses.

2. Equations of motion

Consider a flexible disk fixed to a shaft with angular misalignment, which is illustrated in Fig. 1. The disk rotates about the rotation axis or the shaft axis with a rotating speed Ω and a rotating acceleration $\dot{\Omega}$. The rotation axis of the disk is not parallel to the symmetry axis, as shown in Fig. 1. The angular misalignment of the disk is defined by the angle ϕ between the rotation axis and the symmetry axis. Both the XYZ and xyz co-ordinate systems of Fig. 1 are fixed to the disk. Since the Z-axis is parallel to the rotation axis of the disk and the z-axis is perpendicular to the disk, the angular misalignment ϕ can also be defined by the angle between the Z- and z-axis. This angle is the same as the tilting angle measured from the XY plane to the x-axis. Assuming that the angular misalignment is small, the inner boundary of the disk may be regarded as a circle. Hence, the disk is fixed at the inner radius $r = a$ and free at the outer radius $r = b$, as shown in Fig. 1(c).

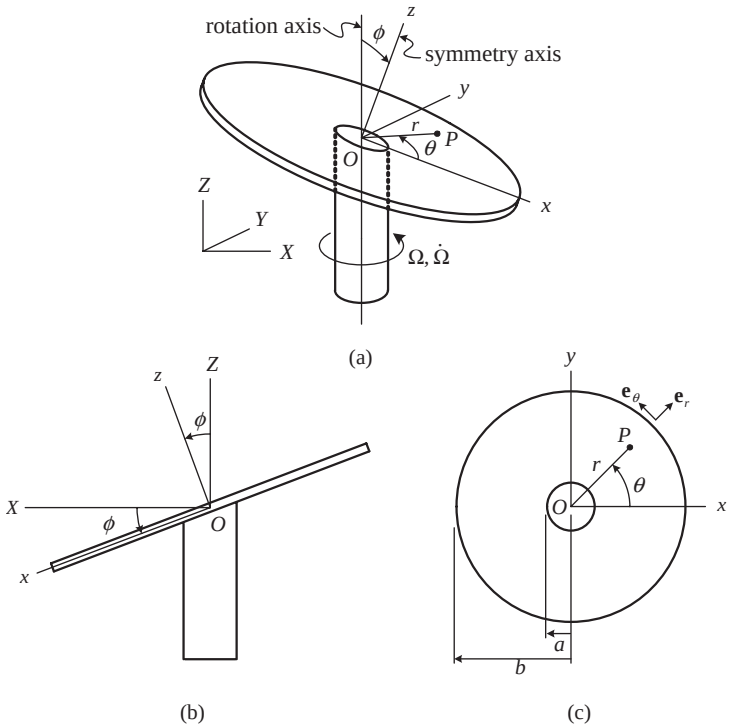

Fig. 1. Schematics of a rotating disk with angular misalignment: (a) a three-dimensional view; (b) a view in the y direction; and (c) a view in the z direction.

The position of point P inside the disk is defined by the radial co-ordinate r and the tangential co-ordinate θ and the transverse co-ordinate z. It is noted that the tangential co-ordinate is measured with respect to the xyz co-ordinate system.

The displacement of point P can be represented by the radial displacement u_r, the tangential displacement u_θ and the transverse displacement u_z. Using the Kirchhoff plate theory, these displacements are expressed in terms of the displacements for a point on the middle surface of the disk:

$$u_r = u - z\frac{\partial w}{\partial r}, \quad u_\theta = v - z\frac{\partial w}{r\partial \theta}, \quad u_z = w, \tag{1}$$

where u, v and w are the radial, tangential and transverse displacements of a point on the middle surface of the disk, respectively. Note that u, v and w are functions of time t as well as the co-ordinates r and θ.

The kinetic energy of the flexible rotating disk needs to be expressed in terms of the displacements and the rotating speed. The position vector of point P is

$$\mathbf{r} = (r + u_r)\mathbf{e}_r + u_\theta \mathbf{e}_\theta + u_z \mathbf{e}_z, \tag{2}$$

where $\mathbf{e}_r$, $\mathbf{e}_\theta$ and $\mathbf{e}_z$ are the unit vectors in the r, θ and z directions. When the shaft rotates with the rotating speed Ω, the angular velocity of the disk, $\boldsymbol{\omega}$, is given by

$$\boldsymbol{\omega} = \Omega(-\sin\phi\cos\theta\mathbf{e}_r + \sin\phi\sin\theta\mathbf{e}_\theta + \cos\phi\mathbf{e}_z). \tag{3}$$

Using Eqs. (1)–(3), the velocity vector of point P, $\mathbf{v}$, can be given by

$$\mathbf{v} = \mathbf{v}_p - z\mathbf{v}_b, \tag{4}$$

where

$$\mathbf{v}_p = \left[\frac{\partial u}{\partial t} + \Omega(-v\cos\phi + w\sin\phi\sin\theta)\right]\mathbf{e}_r + \left\{\frac{\partial v}{\partial t} + \Omega[(r+u)\cos\phi + w\sin\phi\cos\theta]\right\}\mathbf{e}_\theta + \left\{\frac{\partial w}{\partial t} - \Omega[(r+u)\sin\phi\sin\theta + v\sin\phi\cos\theta]\right\}\mathbf{e}_z, \tag{5}$$

$$\mathbf{v}_b = \left(-\frac{\partial^2 w}{\partial t\partial r} + \Omega\frac{\partial w}{r\partial\theta}\cos\phi\right)\mathbf{e}_r - \left(\frac{\partial^2 w}{r\partial t\partial\theta} + \Omega\frac{\partial w}{\partial r}\cos\phi\right)\mathbf{e}_\theta + \Omega\left(\frac{\partial w}{r\partial\theta}\sin\phi\cos\theta + \frac{\partial w}{\partial r}\sin\phi\sin\theta\right)\mathbf{e}_z. \tag{6}$$

Assuming that the disk thickness is small, the kinetic energy of the rotating disk may be approximate to

$$T = \tfrac{1}{2}\rho h\int_A \mathbf{v}_p\cdot\mathbf{v}_p\,\mathrm{d}A, \tag{7}$$

where ρ is the mass density of the disk, h is the thickness, and A is the area.

The potential energy of the disk may be given by

$$U = \frac{1}{2}\int_A \boldsymbol{\varepsilon}^{\mathrm{T}}\boldsymbol{\sigma}\,\mathrm{d}A, \tag{8}$$

where $\boldsymbol{\varepsilon}$ is the strain vector and $\boldsymbol{\sigma}$ is the stress vector. Using the von Karman strain theory, the stress vector can be expressed as

$$\boldsymbol{\varepsilon} = \begin{Bmatrix} \boldsymbol{\varepsilon}_p^L + \boldsymbol{\varepsilon}_p^N \\ \boldsymbol{\varepsilon}_b^L \end{Bmatrix}, \tag{9}$$

where the superscripts L and N represent linear and non-linear terms, respectively, and the subscripts p and b represent the in-plane and bending contributions; $\boldsymbol{\varepsilon}_p^L$, $\boldsymbol{\varepsilon}_p^N$ and $\boldsymbol{\varepsilon}_b^L$ are given by

$$\boldsymbol{\varepsilon}_p^L = \left\{\frac{\partial u}{\partial r}, \frac{\partial v}{r\partial\theta} + \frac{u}{r}, \frac{\partial u}{r\partial\theta} + \frac{\partial v}{\partial r} - \frac{v}{r}\right\}^{\mathrm{T}}, \quad \boldsymbol{\varepsilon}_p^N = \left\{\frac{1}{2}\left(\frac{\partial w}{\partial r}\right)^2, \frac{1}{2}\left(\frac{\partial w}{r\partial\theta}\right)^2, \frac{\partial w}{\partial r}\frac{\partial w}{r\partial\theta}\right\}^{\mathrm{T}},$$

$$\boldsymbol{\varepsilon}_b^L = \left\{-\frac{\partial^2 w}{\partial r^2}, -\left(\frac{\partial w}{r\partial r} + \frac{\partial^2 w}{r^2\partial\theta^2}\right), -2\left(\frac{\partial^2 w}{r\partial r\partial\theta} - \frac{\partial w}{r^2\partial\theta}\right)\right\}^{\mathrm{T}}. \tag{10}$$

On the other hand, the stress vector may be written as

$$\boldsymbol{\sigma} = \mathbf{D}\boldsymbol{\varepsilon}^L, \tag{11}$$

where

$$\boldsymbol{\sigma} = \begin{Bmatrix} \boldsymbol{\sigma}_p \\ \boldsymbol{\sigma}_b \end{Bmatrix}, \quad \boldsymbol{\varepsilon}^L = \begin{Bmatrix} \boldsymbol{\varepsilon}_p^L \\ \boldsymbol{\varepsilon}_b^L \end{Bmatrix}, \quad \mathbf{D} = \begin{bmatrix} \mathbf{D}_p & \mathbf{0} \\ \mathbf{0} & \mathbf{D}_b \end{bmatrix}. \tag{12}$$

In Eq. (12), $\boldsymbol{\sigma}_p$ and $\boldsymbol{\sigma}_b$ represent the linearized internal force vector and the internal moment vector, given by

$$\boldsymbol{\sigma}_p = \{q_r, q_\theta, q_{r\theta}\}^{\mathrm{T}}, \quad \boldsymbol{\sigma}_b = \{m_r, m_\theta, m_{r\theta}\}^{\mathrm{T}}, \tag{13}$$

and $\mathbf{D}_p$ and $\mathbf{D}_b$ are given by

$$\mathbf{D}_p = D_0 \begin{bmatrix} 1 & v & 0 \\ v & 1 & 0 \\ 0 & 0 & (1-v)/2 \end{bmatrix}, \quad \mathbf{D}_b = D \begin{bmatrix} 1 & v & 0 \\ v & 1 & 0 \\ 0 & 0 & (1-v)/2 \end{bmatrix}, \tag{14}$$

where the extensible rigidity D_0 and the bending rigidity D are defined by

$$D_0 = \frac{Eh}{1-v^2}, \quad D = \frac{Eh^3}{12(1-v^2)}. \tag{15}$$

in which E is Young's modulus and v is the Poisson ratio. In Eqs. (13), the linearized internal forces per unit length (q_r, q_θ and $q_{r\theta}$) and the internal moments per unit length (m_r, m_θ and $m_{r\theta}$) are given by

$$q_r = D_0\left[\frac{\partial u}{\partial r} + v\left(\frac{\partial v}{r\partial\theta} + \frac{u}{r}\right)\right], \quad q_\theta = D_0\left(v\frac{\partial u}{\partial r} + \frac{\partial v}{r\partial\theta} + \frac{u}{r}\right), \quad q_{r\theta} = \frac{1-v}{2}D_0\left(\frac{\partial u}{r\partial\theta} + \frac{\partial v}{\partial r} - \frac{v}{r}\right),$$

$$m_r = -D\left[\frac{\partial^2 w}{\partial r^2} + \frac{v}{r}\left(\frac{\partial w}{\partial r} + \frac{\partial w}{r\partial\theta}\right)\right], \quad m_\theta = -D\left[v\frac{\partial^2 w}{\partial r^2} + \frac{1}{r}\left(\frac{\partial w}{\partial r} + \frac{\partial w}{r\partial\theta}\right)\right],$$

$$m_{r\theta} = -\frac{(1-v)D}{r}\left(\frac{\partial^2 w}{\partial r\partial\theta} - \frac{\partial w}{r\partial\theta}\right). \tag{16}$$

If there exist non-conservative forces, the work done by the non-conservative forces is

$$W_{nc} = \int_A (P_r u + P_\theta v + P_z w)\,\mathrm{d}A, \tag{17}$$

where P_r, P_θ and P_z are non-conservative forces in the r, θ and z direction, respectively.

Using the kinetic energy of Eq. (7), the potential energy of Eq. (8) and the non-conservative work of Eq. (17), Hamilton's principle provides the equations of motion and the associated boundary conditions. When the flexible rotating disk has angular misalignment ϕ, the equations of motion are given by

$$\begin{aligned} &\rho h\left[\frac{\partial^2 u}{\partial t^2} - 2\Omega\frac{\partial v}{\partial t}\cos\phi + 2\Omega\frac{\partial w}{\partial t}\sin\phi\sin\theta - \Omega^2(1-\sin^2\phi\cos^2\theta)u\right. \\ &\left. - (\Omega^2\sin^2\phi\cos\theta\sin\theta + \dot{\Omega}\cos\phi)v - (\Omega^2\cos\phi\cos\theta - \dot{\Omega}\sin\theta)w\sin\phi\right] \\ &- \frac{\partial q_r}{\partial r} - \frac{\partial q_{r\theta}}{r\partial\theta} - \frac{q_r - q_\theta}{r} = \rho h\Omega^2 r(1-\sin^2\phi\cos^2\theta) + P_r, \end{aligned} \tag{18}$$

$$\rho h\left[\frac{\partial^2 v}{\partial t^2}+2\Omega\frac{\partial u}{\partial t}\cos\phi+2\Omega\frac{\partial w}{\partial t}\sin\phi\cos\theta-(\Omega^2\sin^2\phi\cos\theta\sin\theta-\dot{\Omega}\cos\phi)u\right.$$
$$\left.-\ \Omega^2(1-\sin^2\phi\sin^2\theta)v+(\Omega^2\cos\phi\sin\theta+\dot{\Omega}\cos\theta)w\sin\phi\right]$$
$$-\frac{\partial q_\theta}{r\partial\theta}-\frac{\partial q_{r\theta}}{\partial r}-2\frac{q_{r\theta}}{r}=\rho hr(\Omega^2\sin^2\phi\sin\theta\cos\theta-\dot{\Omega}\cos\phi)+P_\theta, \tag{19}$$

$$\rho h\left[\frac{\partial^2 w}{\partial t^2}-2\Omega\frac{\partial u}{\partial t}\sin\phi\sin\theta-2\Omega\frac{\partial v}{\partial t}\sin\phi\cos\theta-(\Omega^2\cos\phi\cos\theta+\dot{\Omega}\sin\theta)u\sin\phi\right.$$
$$\left.+\ (\Omega^2\cos\phi\sin\theta-\dot{\Omega}\cos\theta)v\sin\phi-\Omega^2 w\sin^2\phi\right]+D\nabla^4 w-\frac{\partial}{r\partial r}\left[r\left(q_r\frac{\partial w}{\partial r}+q_{r\theta}\frac{\partial w}{r\partial\theta}\right)\right]$$
$$-\frac{\partial}{r\partial\theta}\left(q_{r\theta}\frac{\partial w}{\partial r}+q_\theta\frac{\partial w}{r\partial\theta}\right)=\rho hr(\Omega^2\cos\phi\cos\theta+\dot{\Omega}\sin\theta)\sin\phi+P_z, \tag{20}$$

where

$$\nabla^2=\frac{\partial^2}{\partial r^2}+\frac{\partial}{r\partial r}+\frac{\partial^2}{r^2\partial\theta^2}. \tag{21}$$

The corresponding boundary conditions are the same as those of a conventional rotating disk. The boundary conditions are

$$u=0,\quad v=0,\quad w=0,\quad \frac{\partial w}{\partial r}=0\quad \text{at } r=a, \tag{22}$$

$$q_r=0,\quad q_{r\theta}=0,\quad m_r=0,\quad -D\frac{\partial\nabla^2 w}{\partial r}+\frac{\partial m_{r\theta}}{r\partial\theta}=0\quad \text{at } r=b. \tag{23}$$

Eqs. (18)–(20) represent the equations of motion that predominantly govern the radial, tangential and transverse motions when the rotating disk possesses the angular misalignment. Note that Eqs. (18) and (19) are linear but Eq. (20) is non-linear because q_r, q_θ and $q_{r\theta}$ are functions of u and v. It is interesting that the radial, tangential and transverse motions are fully coupled in Eqs. (18)–(20). Hence, the transverse displacement influences the radial and tangential displacements. This is not observed in a rotating disk with translational misalignment. When a rotating disk has translational misalignment instead of the angular misalignment, the radial and tangential motions are governed by only the radial and tangential displacements while the transverse motion is governed by all the displacements, namely, the radial, tangential and transverse displacements. Therefore, in the case of a disk with the translational misalignment, the transverse motion does not have an effect on the radial and tangential motions. If the angular misalignment is equal to zero, i.e., $\phi=0$, Eqs. (18)–(20) reduce to

$$\rho h\left(\frac{\partial^2 u}{\partial t^2}-2\Omega\frac{\partial v}{\partial t}-\Omega^2 u-\dot{\Omega}v\right)-\frac{\partial q_r}{\partial r}-\frac{\partial q_{r\theta}}{r\partial\theta}-\frac{q_r-q_\theta}{r}=\rho h\Omega^2 r+P_r, \tag{24}$$

$$\rho h\left(\frac{\partial^2 v}{\partial t^2}+2\Omega\frac{\partial u}{\partial t}+\dot{\Omega}u-\Omega^2 v\right)-\frac{\partial q_\theta}{r\partial\theta}-\frac{\partial q_{r\theta}}{\partial r}-2\frac{q_{r\theta}}{r}=-\rho hr\dot{\Omega}+P_\theta, \tag{25}$$

$$\rho h\frac{\partial^2 w}{\partial t^2}+D\nabla^4 w-\frac{\partial}{r\partial r}\left[r\left(q_r\frac{\partial w}{\partial r}+q_{r\theta}\frac{\partial w}{r\partial\theta}\right)\right]-\frac{\partial}{r\partial\theta}\left(q_{r\theta}\frac{\partial w}{\partial r}+q_\theta\frac{\partial w}{r\partial\theta}\right)=P_z. \tag{26}$$

These equations are the same as those for Ref. [11] when the translation misalignment is zero. See Ref. [11] for the details of the equations of motion for a rotating disk with translational misalignment.

3. Finite element formulation

The finite element formulation is used in order to obtain approximate solutions from the partial differential equations of motions. The finite element method is one of the most useful tools to discretize partial differential equations to ordinary differential equations. It is not easy to find the comparison functions that satisfy both the essential and natural boundary conditions given by Eqs. (22) and (23). This study adopts the finite element method that uses the admissible functions often called the shape functions instead of the comparison functions. Since the admissible functions may satisfy only the essential boundary conditions, the difficulty to find the comparison functions can be avoided.

The trial and weighting functions need to be defined before deriving the weak form. The trial functions are functions in the Hilbert space H^1, which satisfy both the essential and natural boundary conditions. Denoting the trial functions in the r, θ and z directions by u, v and w, they can be defined as follows:

$$(u,v)\in V_{uv}=\{(u,v)\,|\,u\in H^1, v\in H^1, u|_{r=a}=0, v|_{r=a}=0, q_r|_{r=b}=0, q_{r\theta}|_{r=b}=0\}, \tag{27}$$

$$\begin{aligned} w\in V_w=\{w\,|\,w\in H^1, \partial w/\partial r\in H^1, \partial w/\partial\theta\in H^1, w|_{r=a}=0, \partial w/\partial r|_{r=a}=0, m_r|_{r=b}=0,\\ -D\partial\nabla^2 w/\partial r+\partial m_{r\theta}/r\partial\theta|_{r=b}=0\}, \end{aligned} \tag{28}$$

where V_{uv} is the trial function space for the radial and tangential displacements and V_w is the one for the transverse displacement. Eq. (28) implies that both the transverse displacement and its derivatives should be in the Hilbert space. This is because the displacement as well as the slopes should be described as degrees of freedom in the plate theory of the finite element method. The weighting function is defined as an arbitrary function, which is zero on the boundary where the essential boundary conditions are prescribed. Therefore, the weighting functions for the radial, tangential and transverse displacements, which are represented by $\bar{u}$, $\bar{v}$ and $\bar{w}$, are given by

$$(\bar{u},\bar{v})\in \bar{V}_{uv}=\{(\bar{u},\bar{v})\,|\,\bar{u}\in H^1, \bar{v}\in H^1, \bar{u}|_{r=a}=0, \bar{v}|_{r=a}=0\}, \tag{29}$$

$$\bar{w}\in \bar{V}_w=\{\bar{w}\,|\,\bar{w}\in H^1, \partial\bar{w}/\partial r\in H^1, \partial\bar{w}/\partial\theta\in H^1, \bar{w}|_{r=a}=0, \partial\bar{w}/\partial r|_{r=a}=0\}. \tag{30}$$

As the first step of the finite element formulation, the weak form should be derived from the strong form given by the partial differential equations (18)–(20) and the associated boundary conditions given by Eqs. (22) and (23). Since Eqs. (18)–(20) are fully coupled with each other, only one weak form is derived. The weak form is obtained by multiplying Eqs. (18)–(20) by the weighting functions $\bar{u}$, $\bar{v}$ and $\bar{w}$, respectively, summing the equations, and then integrating the resultant equation over the disk area A with the divergence theorem. The weak form can be

expressed as

$$\rho h \int_A \bar{\mathbf{u}}^{\mathrm{T}} \frac{\partial^2 \mathbf{u}}{\partial t^2}\,\mathrm{d}A + 2\Omega\rho h \int_A \bar{\mathbf{u}}^{\mathrm{T}} \boldsymbol{\Phi}_g \frac{\partial \mathbf{u}}{\partial t}\,\mathrm{d}A - \Omega^2 \rho h \int_A \bar{\mathbf{u}}^{\mathrm{T}} \boldsymbol{\Phi}_k \mathbf{u}\,\mathrm{d}A + \dot{\Omega}\rho h \int_A \bar{\mathbf{u}}^{\mathrm{T}} \boldsymbol{\Phi}_g \mathbf{u}\,\mathrm{d}A + \int_A (\bar{\boldsymbol{\varepsilon}}^L)^{\mathrm{T}} \mathbf{D}\boldsymbol{\varepsilon}^L\,\mathrm{d}A + \int_A \bar{\boldsymbol{\theta}}^{\mathrm{T}} \mathbf{Q}\boldsymbol{\theta}\,\mathrm{d}A = \int_A \bar{\mathbf{u}}^{\mathrm{T}} \mathbf{f}\,\mathrm{d}A, \tag{31}$$

where

$$\mathbf{u} = \begin{Bmatrix} u \\ v \\ w \end{Bmatrix}, \quad \bar{\mathbf{u}} = \begin{Bmatrix} \bar{u} \\ \bar{v} \\ \bar{w} \end{Bmatrix}, \quad \boldsymbol{\theta} = \begin{Bmatrix} \dfrac{\partial w}{\partial r} \\ \dfrac{\partial w}{r\partial\theta} \end{Bmatrix}, \quad \bar{\boldsymbol{\theta}} = \begin{Bmatrix} \dfrac{\partial \bar{w}}{\partial r} \\ \dfrac{\partial \bar{w}}{r\partial\theta} \end{Bmatrix},$$

$$\bar{\boldsymbol{\varepsilon}}^L = \left\{ \frac{\partial \bar{u}}{\partial r}, \frac{\partial \bar{v}}{r\partial\theta} + \frac{\bar{u}}{r}, \frac{\partial \bar{u}}{r\partial\theta} + \frac{\partial \bar{v}}{\partial r} - \frac{\bar{v}}{r}, -\frac{\partial^2 \bar{w}}{\partial r^2}, -\frac{1}{r}\left(\frac{\partial \bar{w}}{\partial r} + \frac{\partial^2 \bar{w}}{r\partial\theta^2}\right), -\frac{2}{r}\left(\frac{\partial^2 \bar{w}}{\partial r\partial\theta} - \frac{\partial \bar{w}}{r\partial\theta}\right) \right\}^{\mathrm{T}},$$

$$\boldsymbol{\Phi}_g = \begin{bmatrix} 0 & -\cos\phi & \sin\phi\sin\theta \\ \cos\phi & 0 & \sin\phi\cos\theta \\ -\sin\phi\sin\theta & -\sin\phi\cos\theta & 0 \end{bmatrix},$$

$$\boldsymbol{\Phi}_k = \begin{bmatrix} 1-\sin^2\phi\cos^2\theta & \sin^2\phi\cos\theta\sin\theta & \cos\phi\sin\phi\cos\theta \\ \sin^2\phi\cos\theta\sin\theta & 1-\sin^2\phi\sin^2\theta & -\cos\phi\sin\phi\sin\theta \\ \cos\phi\sin\phi\cos\theta & -\cos\phi\sin\phi\sin\theta & \sin^2\phi \end{bmatrix}, \quad \mathbf{Q} = \begin{bmatrix} q_r & q_{r\theta} \\ q_{r\theta} & q_\theta \end{bmatrix},$$

$$\mathbf{f} = \begin{Bmatrix} \rho h\Omega^2 r(1-\sin^2\phi\cos^2\theta) + P_r \\ \rho h r(\Omega^2 \sin^2\phi\sin\theta\cos\theta - \dot{\Omega}\cos\phi) + P_\theta \\ \rho h r(\Omega^2\cos\phi\cos\theta + \dot{\Omega}\sin\theta)\sin\phi + P_z \end{Bmatrix}. \tag{32}$$

Using the four-node annular sector elements defined in Ref. [11], the trial function vector $\mathbf{u}$ in an element may be presented as

$$\mathbf{u} = \mathbf{N}^{\mathrm{T}}\,\mathbf{d}^e, \tag{33}$$

where $\mathbf{d}^e$ is the element displacement vector and $\mathbf{N}$ is the shape function vector that is a function of r and θ. It should be noted that each node of the element has six degrees of freedom of u, v, w, $\partial w/\partial r$, $\partial w/\partial\theta$ and $\partial^2 w/\partial r\partial\theta$. Therefore, the shape function vector is a 24×3 matrix and element displacement vector is given by

$$\mathbf{d}^e = \{u_1, v_1, w_1, (\partial w/\partial r)_1, (\partial w/\partial\theta)_1, (\partial^2 w/\partial r\partial\theta)_1, \ldots, u_4, v_4, w_4, (\partial w/\partial r)_4, (\partial w/\partial\theta)_4, (\partial^2 w/\partial r\partial\theta)_4\}^{\mathrm{T}}. \tag{34}$$

Similarly, the $\boldsymbol{\theta}$ vector in Eqs. (32) can be written as

$$\boldsymbol{\theta} = \mathbf{N}_\theta^{\mathrm{T}}\mathbf{d}^e, \tag{35}$$

where $\mathbf{N}_\theta$ is a 24×3 matrix that is also a function of r and θ. On the other hand, introducing Eq. (33) into the second equation of Eqs. (12), the linearized strain is given by

$$\boldsymbol{\varepsilon}^L = \mathbf{B}\mathbf{d}^e, \tag{36}$$

where $\mathbf{B}$ is a 24×6 matrix. The weighting function vectors $\bar{\mathbf{u}}$, $\bar{\boldsymbol{\theta}}$ and $\bar{\boldsymbol{\varepsilon}}^L$ are given by

$$\bar{\mathbf{u}} = \mathbf{N}^{\mathrm{T}}\bar{\mathbf{d}}^e, \quad \bar{\boldsymbol{\theta}} = \mathbf{N}_\theta^{\mathrm{T}}\bar{\mathbf{d}}^e, \quad \bar{\boldsymbol{\varepsilon}}^L = \mathbf{B}\bar{\mathbf{d}}^e, \tag{37}$$

where $\bar{\mathbf{d}}^e$ is an arbitrary 24×1 vector.

The next step of the finite element formulation is the spatial discretization of the weak form. After the disk area A is discretized by using N_e elements, substitution of Eqs. (33) and (35)–(37) in Eq. (31) results in

$$\sum_{e=1}^{N_e} (\bar{\mathbf{d}}^e)^{\mathrm{T}}\{\mathbf{m}^e\ddot{\mathbf{d}}^e + 2\Omega\mathbf{g}^e\dot{\mathbf{d}}^e + [\mathbf{k}^e - \Omega^2\mathbf{m}_\Phi^e + \dot{\Omega}\mathbf{g}_\Phi^e]\mathbf{d}^e + \mathbf{p}^e\} = \sum_{e=1}^{N_e} (\bar{\mathbf{d}}^e)^{\mathrm{T}}\mathbf{f}^e, \tag{38}$$

where

$$\mathbf{m}^e = \rho h \int_{A_e} \mathbf{N}\mathbf{N}^{\mathrm{T}}\,\mathrm{d}A, \quad \mathbf{g}^e = \rho h \int_{A_e} \mathbf{N}\boldsymbol{\Phi}_g\mathbf{N}^{\mathrm{T}}\,\mathrm{d}A, \quad \mathbf{k}^e = \int_{A_e} \mathbf{B}^{\mathrm{T}}\mathbf{D}\mathbf{B}\,\mathrm{d}A,$$

$$\mathbf{m}_\Phi^e = \rho h \int_{A_e} \mathbf{N}\boldsymbol{\Phi}_k\mathbf{N}^{\mathrm{T}}\,\mathrm{d}A,$$

$$\mathbf{g}_\Phi^e = \rho h \int_{A_e} \mathbf{N}\boldsymbol{\Phi}_g\mathbf{N}^{\mathrm{T}}\,\mathrm{d}A, \quad \mathbf{p}^e = \left(\int_{A_e} \mathbf{N}_\theta\mathbf{Q}\mathbf{N}_\theta^{\mathrm{T}}\,\mathrm{d}A\right)\mathbf{d}^e, \quad \mathbf{f}^e = \int_{A_e} \mathbf{N}\mathbf{f}\,\mathrm{d}A, \tag{39}$$

in which A_e is the element area. All the matrices in Eqs. (39) are 24×24 matrices while the element internal force vector $\mathbf{p}^e$ and the element load vector $\mathbf{f}^e$ are 24×1 vectors. Note that the element internal force vector is a non-linear function of the element displacement vector $\mathbf{d}^e$, because the elements of $\mathbf{Q}$ are functions of u_i and v_i where $i = 1, 2, 3$, and 4.

Through the assembling procedure, a set of ordinary differential equations can be obtained in matrix–vector form. Since $\bar{\mathbf{d}}^e$ is an arbitrary vector, by assembling the element matrices and vectors, Eq. (38) can be written as the global matrix–vector equation. The global equation is given by

$$\mathbf{M}\ddot{\mathbf{d}} + 2\Omega\mathbf{G}\dot{\mathbf{d}} + [\mathbf{K} - \Omega^2\mathbf{M}_\Phi + \dot{\Omega}\mathbf{G}_\Phi]\,\mathbf{d} + \mathbf{P}(\mathbf{d}) = \mathbf{F}, \tag{40}$$

where $\mathbf{d}$ is the global displacement vector, $\mathbf{M}$ is the global mass matrix, $\mathbf{G}$ is the global gyroscopic matrix, $\mathbf{K}$ is the global stiffness matrix, $\mathbf{M}_\Phi$ is the global motion-induced mass matrix, $\mathbf{G}_\Phi$ is the global motion-induced gyroscopic matrix, $\mathbf{P}(\mathbf{d})$ is the non-linear global internal force vector due to the membrane stresses, and $\mathbf{F}$ is the global load vector. These matrices and vectors are defined by

$$\mathbf{d} = \{u_1, v_1, w_1, (\partial w/\partial r)_1, (\partial w/\partial\theta)_1, (\partial^2 w/\partial r\partial\theta)_1, \ldots, u_{N_e+1}, v_{N_e+1}, w_{N_e+1}, (\partial w/\partial r)_{N_e+1}, (\partial w/\partial\theta)_{N_e+1}, (\partial^2 w/\partial r\partial\theta)_{N_e+1}\}^{\mathrm{T}}, \tag{41}$$

$$\mathbf{M} = \mathop{\mathrm{A}}_{e=1}^{N_e} \mathbf{m}^e, \quad \mathbf{G} = \mathop{\mathrm{A}}_{e=1}^{N_e} \mathbf{g}^e, \quad \mathbf{K} = \mathop{\mathrm{A}}_{e=1}^{N_e} \mathbf{k}^e, \quad \mathbf{M}_\Phi = \mathop{\mathrm{A}}_{e=1}^{N_e} \mathbf{m}_\Phi^e, \quad \mathbf{G}_\Phi = \mathop{\mathrm{A}}_{e=1}^{N_e} \mathbf{g}_\Phi^e,$$

$$\mathbf{P} = \mathop{\mathrm{A}}_{e=1}^{N_e} \mathbf{p}^e, \quad \mathbf{F} = \mathop{\mathrm{A}}_{e=1}^{N_e} \mathbf{f}^e, \tag{42}$$

where A denotes the assembly operator. When the number of the discretized elements is N_e, the sizes of $\mathbf{d}$, $\mathbf{P}$ and $\mathbf{F}$ are $6(N_e+1)\times 1$ and the sizes of $\mathbf{M}$, $\mathbf{G}$, $\mathbf{K}$, $\mathbf{M}_\Phi$ and $\mathbf{G}_\Phi$ are $6(N_e+1)\times 6(N_e+1)$. It should be noted again that Eq. (40) is a non-linear equation because $\mathbf{P}$ is a function of $\mathbf{d}$.

4. Natural frequencies and mode shapes

In order to obtain the natural frequencies and mode shapes of the rotating disk with angular misalignment, the non-linear equation of motion given by Eq. (40) is linearized by the perturbation method. In the neighbourhood of an equilibrium position, Eq. (40) is linearized assuming that the motion of the disk is in a dynamic steady state, i.e., $\dot{\Omega}=0$. Denoting the displacement vector of the equilibrium position by $\mathbf{d}^*$ and a perturbed displacement vector from the equilibrium position by $\Delta\mathbf{d}$, the displacement vector can be written as

$$\mathbf{d}=\mathbf{d}^*+\Delta\mathbf{d}. \tag{43}$$

Substitution of Eq. (43) into Eq. (40) produces a dynamic equilibrium equation in a steady state and a perturbed equation from the equilibrium position. The equilibrium equation is given by

$$[\mathbf{K}-\Omega^2\mathbf{M}_\Phi]\mathbf{d}^*+\mathbf{P}(\mathbf{d}^*)=\mathbf{F}, \tag{44}$$

where the global load vector $\mathbf{F}$ is computed when $\dot{\Omega}=0$. Since Eq. (44) is non-linear, the equilibrium position vector $\mathbf{d}^*$ can be obtained by a non-linear equation solver, e.g., the Newton–Raphson method. The perturbed equation may be expressed as

$$\mathbf{M}\Delta\ddot{\mathbf{d}}+2\Omega\mathbf{G}\Delta\dot{\mathbf{d}}+[\mathbf{K}+\mathbf{K}_T-\Omega^2\mathbf{M}_\Phi]\Delta\mathbf{d}=\mathbf{0}, \tag{45}$$

where $\mathbf{K}_T$ is the tangent matrix at the equilibrium position, defined by

$$\mathbf{K}_T=\left.\frac{\partial\mathbf{P}}{\partial\mathbf{d}}\right|_{\mathbf{d}=\mathbf{d}^*}. \tag{46}$$

From the perturbed equation (45), the eigenvalue problems are derived, from which the natural frequencies and mode shapes can be computed. Assume a solution of Eqs. (45) as

$$\Delta\mathbf{d}=\mathbf{X}e^{i\omega_n t}, \tag{47}$$

where $i=\sqrt{-1}$; ω_n is the natural frequency; and $\mathbf{X}$ is the modal vector. Substitution of Eq. (47) into Eq. (45) leads to the eigenvalue problems given by

$$[\mathbf{K}+\mathbf{K}_T-\Omega^2\mathbf{M}_\Phi-\omega_n^2\mathbf{M}+2i\omega_n\Omega\mathbf{G}]\mathbf{X}=\mathbf{0}. \tag{48}$$

To verify the equations of motion derived in this study, convergence tests for the natural frequencies are performed. The dimensions and material properties of a disk used in computations of this paper are $a=0.015$ m, $b=0.065$ m, $h=0.0012$ m, $\rho=1200$ kg/m^3, $v=0.3$ and $E=65.5\times10^6$ N/m^2. The equations of motion (24)–(26) when there is no angular misalignment, i.e., $\phi=0^\circ$, are identical to the equations of Ref. [11] when there is no translational misalignment, i.e., $\varepsilon=0$. Therefore, there is no need to check the convergence of the natural frequencies when a disk without angular misalignment has a constant rotating speed. Tables 1 and 2 present the convergence characteristics of the natural frequencies when the disk has $\phi=2^\circ$ and

Table 1
Convergence characteristics of the natural frequencies (rad/s) for the out-of-plane motion when $\phi = 2^\circ$, $\Omega = 1000$ rad/s and $\dot{\Omega} = 0$ rad/s^2

M	N	Mode				
		(0,0)	$(0,1)_s$	$(0,1)_a$	$(0,2)_s$	$(0,2)_a$
	4	964.8201	1060.7303	1140.6227	1532.2139	1538.3722
	8	964.8136	1060.7141	1140.6195	1531.4162	1532.0282
4	12	964.8016	1060.7134	1140.6138	1531.2321	1531.9314
	16	964.7761	1060.7121	1140.6023	1531.1996	1531.9267
	20	964.7053	1060.7095	1140.5756	1531.1890	1531.9256
	24	964.3757	1060.7031	1140.4886	1531.1841	1531.9249
	4	955.0362	1049.3734	1134.4084	1529.7274	1535.9080
	8	955.0294	1049.3592	1134.4054	1528.9221	1529.5430
6	12	955.0169	1049.3584	1134.4002	1528.7390	1529.4421
	16	954.9903	1049.3569	1134.3897	1528.7073	1529.4334
	20	954.9164	1049.3540	1134.3653	1528.6972	1529.4333
	24	954.5752	1049.3470	1134.2848	1528.6926	1529.4329
	4	951.0032	1044.6439	1131.7349	1528.3022	1534.4869
	8	950.9962	1044.6306	1131.7321	1527.4929	1533.7047
8	12	950.9835	1044.6298	1131.7270	1527.3105	1528.1195
	16	950.9563	1044.6283	1131.7168	1527.2792	1528.0166
	20	950.8810	1044.6252	1131.6935	1527.2693	1528.0068
	24	950.5346	1044.6180	1131.6155	1527.2649	1528.0058
	4	949.0614	1042.2929	1130.4224	1527.5195	1528.0057
	8	949.0544	1042.2801	1130.4196	1526.7078	1527.3380
10	12	949.0415	1042.2792	1130.4146	1526.5258	1527.2339
	16	949.0141	1042.2777	1130.4046	1526.4948	1527.2236
	20	948.9381	1042.2746	1130.3817	1526.4850	1527.2222
	24	948.5888	1042.2672	1130.3050	1526.4807	1527.2221

$\Omega = 1000$ rad/s. In Tables 1 and 2, M and N stand for the numbers of elements in the radial and tangential directions and the mode (m,n) represents a mode with m nodal circles and n nodal diameters. The subscripts s and a of Table 1 denote the symmetric and asymmetric modes, respectively, while the subscripts f and b of Table 2 denote the forward and backward travelling modes. Tables 1 and 2 present the convergence characteristics of the natural frequencies of the out-of-plane and in-plane motions, respectively. Since the natural frequencies computed from Eq. (48) involve both the in-plane and out-of-plane natural frequencies, the computed frequencies need to be sorted into the in-plane and out-of-plane natural frequencies. When the angular misalignment is small, this sorting can be performed by examining the mode shapes of the corresponding natural frequencies. However, it may be impossible to distinguish between the in-plane and out-of-plane modes if the angular misalignment is large. As shown in Tables 1 and 2, the natural frequencies of the in-plane and out-of-plane motions converge as the number of elements increases. It is also shown that the natural frequencies when $M = 10$ and $N = 24$ are

Table 2
Convergence characteristics of the natural frequencies (rad/s) for the in-plane motion when $\phi = 2^\circ$, $\Omega = 1000$ rad/s and $\dot{\Omega} = 0$ rad/s^2

M	N	Mode				
		$(0,0)$	$(0,1)_b$	$(0,1)_f$	$(0,2)_b$	$(0,2)_f$
	4	1273.2136	2996.8148	6141.9265	9294.4430	17195.263
	8	1273.1825	2974.2066	4429.9796	5968.5759	8357.9495
4	12	1273.1821	2930.2839	4391.7360	5596.4974	7446.1026
	16	1273.1816	2903.7753	4360.0797	5463.6628	7254.7026
	20	1273.1805	2894.9633	4345.5518	5347.3738	7110.8778
	24	1273.1787	2891.3606	4337.6933	5302.6313	6896.3085
	4	1262.5498	2959.3927	6040.2772	9182.1903	15457.608
	8	1262.5187	2958.8675	4394.7380	5921.6181	8240.2810
6	12	1262.5184	2899.8877	4379.4302	5491.4095	7383.7389
	16	1262.5178	2871.7581	4347.4811	5410.6356	7198.9481
	20	1262.5169	2861.4757	4332.8192	5292.5268	7053.1921
	24	1262.5152	2857.0462	4324.8883	5230.0615	6839.8444
	4	1258.4500	2940.3418	6005.5051	9142.1340	15094.899
	8	1258.4189	2939.8146	4377.3165	5901.7135	8178.0022
8	12	1258.4186	2888.1023	4374.4891	5451.8180	7356.0285
	16	1258.4181	2858.9173	4342.4250	5390.9092	7178.2802
	20	1258.4171	2847.4414	4327.7104	5272.1610	7029.1496
	24	1258.4156	2842.2156	4319.7512	5209.1050	6816.2104
	4	1256.4897	2930.2369	5987.4753	9123.4327	15013.119
	8	1256.4586	2929.7096	4368.1706	5890.8483	8147.6240
10	12	1256.4583	2882.3995	4367.7959	5431.3377	7341.5137
	16	1256.4578	2852.7457	4339.9162	5381.4159	7166.9528
	20	1256.4569	2840.7042	4325.1759	5262.3574	7016.9214
	24	1256.4554	2835.0448	4317.2028	5199.0738	6804.1855

sufficiently converged. Therefore, the further computations use a finite element model that has 10 and 24 elements in the radial and tangential directions.

First, consider the effects of the rotating speed on the natural frequencies when the disk has angular misalignment. When the disk has angular misalignment $\phi = 2^\circ$, the variations of the natural frequencies for the rotating speed are depicted in Fig. 2. As pointed out before, both the out-of-plane and in-plane natural frequencies are computed simultaneously from Eq. (48). In Fig. 2, the thin lines represent the natural frequencies for the out-of-plane motion and the thick lines for the in-plane motion. In order to investigate the behaviours of the natural frequencies in more detail, only the out-of-plane natural frequencies are presented as functions of the rotating speed in Fig. 3, where the solid lines are for $\phi = 2^\circ$ and the dotted lines for $\phi = 0^\circ$. The mode split phenomenon, which means that one natural frequency is split into two as the rotating speed increases, is observed in the (0,1) mode of Fig. 3. In fact all the modes except the (0,0) mode have mode splits if the rotating disk has angular misalignment. Since the amounts of the frequency

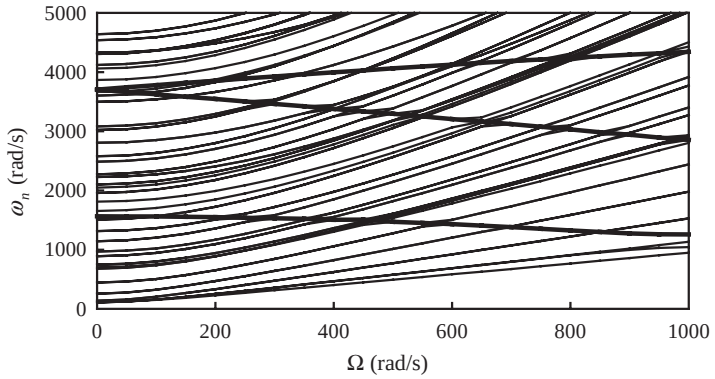

Fig. 2. Variations of the natural frequencies for the rotating speed when the disk has the angular misalignment $\phi = 2^\circ$. The thin lines represent the out-of-plane natural frequencies while the thick lines do the in-plane natural frequencies.

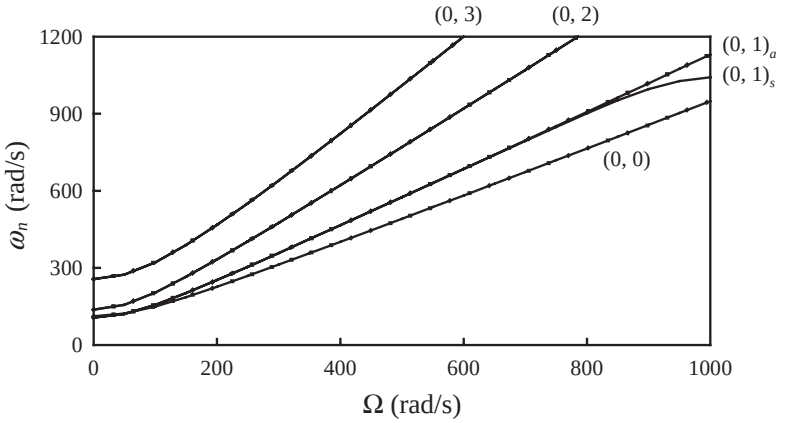

Fig. 3. Variations of the out-of-plane natural frequencies for the rotating speed: ——, $\phi = 2^\circ$; ⋯⋯, $\phi = 0^\circ$.

splits in the (0,2) and (0,3) modes are not significant, it is hard to find the mode splits of those modes in Fig. 3. In order to manifest the frequency splits, Fig. 4 demonstrates the differences between the natural frequencies when $\phi = 2^\circ$ and $\phi = 0^\circ$. These differences are given by $\Delta\omega_n = \omega_n|_{\phi=2^\circ} - \omega_n|_{\phi=0^\circ}$. Compared to the other modes, the (0,1) mode exhibits the largest amount of frequency split as shown in Fig. 4. It is also observed that differences between the natural frequencies of the symmetric and asymmetric modes become large as the rotating speed increases.

Fig. 5 shows the mode shapes of the out-of-plane motion when the disk has the angular misalignment $\phi = 2^\circ$ and the rotating speed $\Omega = 1000$ rad/s. As illustrated in Fig. 5, the symmetric mode shapes are symmetric about the xz plane, but the asymmetric modes are not symmetric. It is interesting that the asymmetric (0,1) and (0,2) modes rotate by approximately 90° and 45° from the symmetric (0,1) and (0,2) modes, respectively. The discussion on the rotation of modes can be found in Ref. [13].

The variations of the in-plane natural frequencies for the rotating speed are presented in Fig. 6, where the solid and dotted lines stand for the natural frequencies when $\phi = 2^\circ$ and $\phi = 0^\circ$,

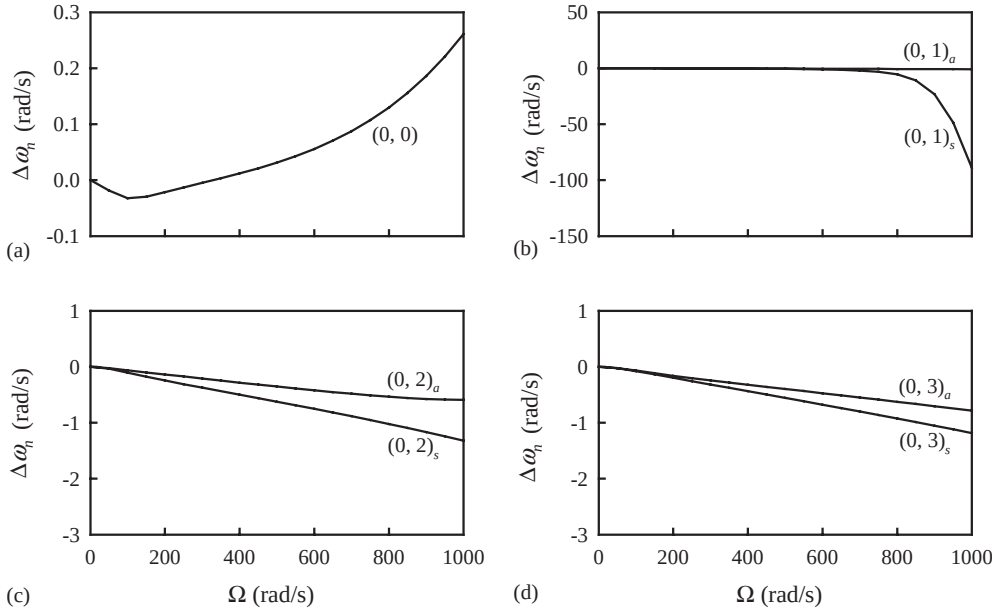

Fig. 4. Differences between the out-of-plane natural frequencies when $\phi = 2^\circ$ and $\phi = 0^\circ$ versus the rotating speed: (a) the (0,0) out-of-plane mode; (b) the (0,1) out-of-plane mode; (c) the (0,2) out-of-plane mode; and (d) the (0,3) out-of-plane mode.

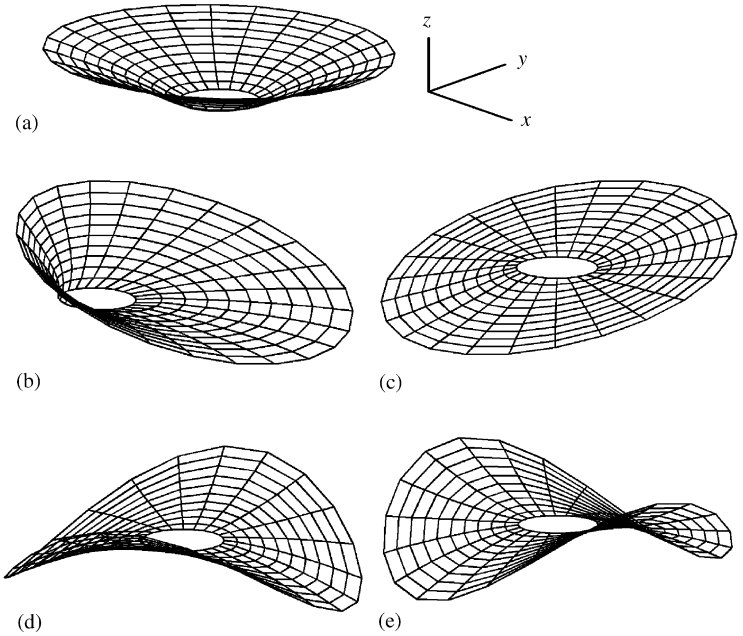

Fig. 5. Mode shapes of the out-of-plane motion when $\phi = 2^\circ$ and $\Omega = 1000$ rad/s: (a) the (0,0) mode; (b) the symmetric (0,1) mode; (c) the asymmetric (0,1) mode; (d) the symmetric (0,2) mode; and (e) the asymmetric (0,2) mode.

respectively. Note that, for the (0,1) or higher in-plane modes with the nodal diameter, the natural frequency split exists regardless of the existence of angular misalignment. In fact, higher in-plane modes, for example, the (0,2) and (0,3) modes show similar natural frequency split as the rotating speed increases. Therefore, the frequency splits in the in-plane modes are not caused by the angular misalignment. These splits result from the gyroscopic effect when the disk rotates. The increasing and decreasing frequencies for the variation of the rotating speed are called the natural frequencies of the forward and backward travelling modes, respectively. Fig. 7 shows the differences between the in-plane natural frequencies when $\phi = 2^\circ$ and $\phi = 0^\circ$ versus the rotating speed. It is interesting that the (0,0) in-plane mode has the largest difference of the natural frequencies between the disks with and without angular misalignment, compared to the $(0,1)_b$ and $(0,1)_f$ modes.

Next, the variations of the out-of-plane natural frequencies for the angular misalignment are investigated. Fig. 8 presents the out-of-plane natural frequencies of the disk with $\Omega = 1000$ rad/s when the angular misalignment varies from 0° to 5°. Fig. 8(a) shows that the natural frequency of the (0,0) out-of-plane mode increases with the angular misalignment. However, as illustrated in

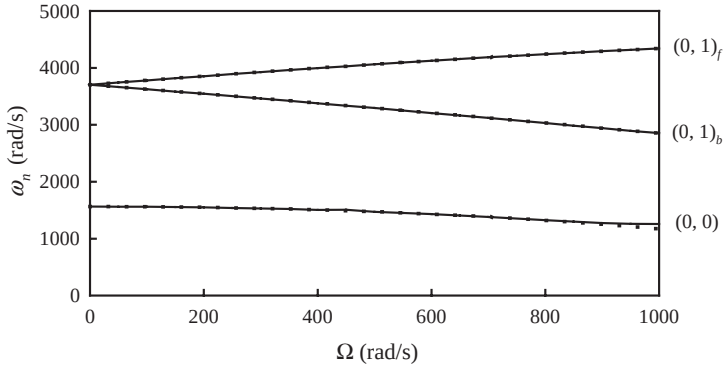

Fig. 6. Variations of the in-plane natural frequencies for the rotating speed: ——, $\phi = 2^\circ$; ⋯⋯, $\phi = 0^\circ$.

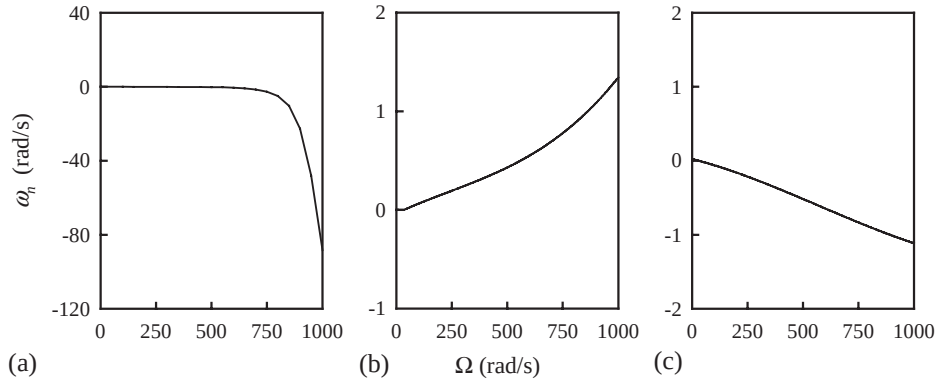

Fig. 7. Differences between the in-plane natural frequencies when $\phi = 2^\circ$ and $\phi = 0^\circ$ versus the rotating speed: (a) the (0,0) in-plane mode; (b) the $(0,1)_b$ in-plane mode; and (c) the $(0,1)_f$ in-plane mode.

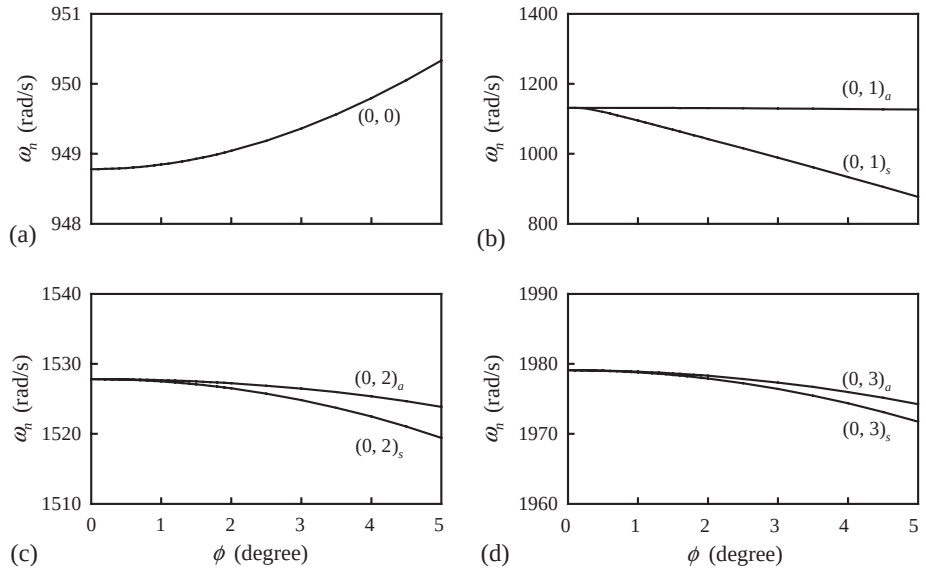

Fig. 8. Variations of the out-of-plane natural frequencies for the angular misalignment when the disk has the rotating speed $\Omega = 1000$ rad/s: (a) the (0,0) out-of-plane mode; (b) the (0,1) out-of-plane mode; (c) the (0,2) out-of-plane mode; and (d) the (0,3) out-of-plane mode.

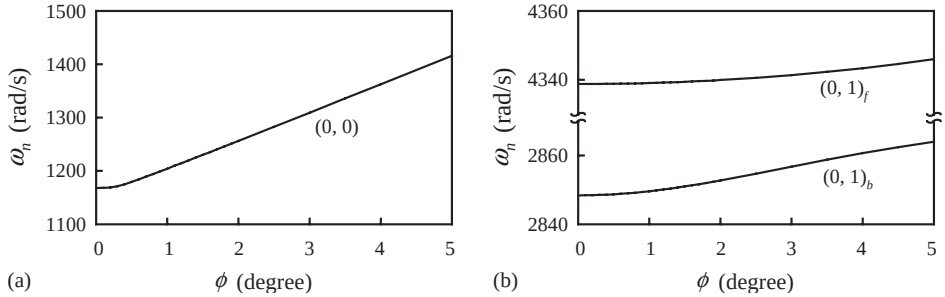

Fig. 9. Variations of the in-plane natural frequencies for the angular misalignment when the disk has the rotating speed $\Omega = 1000$ rad/s: (a) the (0,0) in-plane mode; and (b) the (0,1) in-plane mode.

Figs. 8(b)–(d), the frequencies for the (0,1), (0,2) and (0,3) out-of-plane modes decrease as the misalignment increases. Note that the amounts of the natural frequency splits become large with the angular misalignment. It is also noted that the (0,1) out-of-plane mode has the largest frequency split compared to the other modes. On the other hand, as shown in Fig. 9, the in-plane modes have a trend that the natural frequencies increase with the angular misalignment.

5. Non-linear dynamic responses

The non-linear dynamic responses of the displacements are analyzed when the rotating disk has angular misalignment. The dynamic responses are computed by using the generalized-α time

integration method [12]. In order to apply the generalized-α method to the non-linear equation (40), the equation may be converted to

$$\mathbf{M}\mathbf{a}_{n+1-\alpha_m} + 2\Omega_{n+1-\alpha_f}\mathbf{G}\mathbf{v}_{n+1-\alpha_f} + [\mathbf{K} - \Omega^2_{n+1-\alpha_f}\mathbf{M}_\Phi + \dot{\Omega}_{n+1-\alpha_f}\mathbf{G}_\Phi]\mathbf{d}_{n+1-\alpha_f} + \mathbf{P}(\mathbf{d}_{n+1-\alpha_f}) = \mathbf{F}_{n+1-\alpha_f}, \tag{49}$$

where

$$\mathbf{d}_{n+1-\alpha_f} = (1-\alpha_f)\mathbf{d}_{n+1} + \alpha_f\mathbf{d}_n, \quad \mathbf{v}_{n+1-\alpha_f} = (1-\alpha_f)\mathbf{v}_{n+1} + \alpha_f\mathbf{v}_n, \quad \mathbf{a}_{n+1-\alpha_m} = (1-\alpha_m)\mathbf{a}_{n+1} + \alpha_m\mathbf{a}_n,$$

$$\mathbf{F}_{n+1-\alpha_f} = \mathbf{F}((1-\alpha_f)t_{n+1} + \alpha_f t_n), \quad \Omega_{n+1-\alpha_f} = \Omega((1-\alpha_f)t_{n+1} + \alpha_f t_n),$$

$$\dot{\Omega}_{n+1-\alpha_f} = \dot{\Omega}((1-\alpha_f)t_{n+1} + \alpha_f t_n), \tag{50}$$

in which $\mathbf{d}_n$, $\mathbf{v}_n$ and $\mathbf{a}_n$ are approximated values of $\mathbf{d}$, $\dot{\mathbf{d}}$ and $\ddot{\mathbf{d}}$ at time $t = t_n$; α_m and α_f are the algorithmic parameters of the generalized-α method. The displacement and velocity update equations are given by

$$\mathbf{d}_{n+1} = \mathbf{d}_n + \Delta t\mathbf{v}_n + \Delta t^2[(1/2-\beta)\mathbf{a}_n + \beta\mathbf{a}_{n+1}], \tag{51}$$

$$\mathbf{v}_{n+1} = \mathbf{v}_n + \Delta t[(1-\gamma)\mathbf{a}_n + \gamma\mathbf{a}_{n+1}], \tag{52}$$

where Δt is the time step size given by $\Delta t = t_{n+1} - t_n$, β and γ are the algorithmic parameter given by

$$\beta = \tfrac{1}{4}(1-\alpha_m+\alpha_f)^2, \quad \gamma = \tfrac{1}{2} - \alpha_m + \alpha_f. \tag{53}$$

The initial conditions of this problem may be given by

$$\mathbf{d}_0 = \mathbf{d}(0), \quad \mathbf{v}_0 = \mathbf{v}(0),$$

$$\mathbf{a}_0 = \mathbf{M}^{-1}\{\mathbf{F}(0) - 2\Omega(0)\mathbf{G}\mathbf{v}_0 - [\mathbf{K} - \Omega^2(0)\mathbf{M}_\Phi + \dot{\Omega}(0)\mathbf{G}_\Phi]\mathbf{d}_0 - \mathbf{P}(\mathbf{d}_0)\}. \tag{54}$$

The Newton–Raphson method is used to obtain dynamic responses from the non-linear equation (49). In order to update the displacement and the velocity with known values of $\mathbf{d}_n$, $\mathbf{v}_n$, $\mathbf{a}_n$ and Δt, the acceleration $\mathbf{a}_{n+1}$ should be determined from Eqs. (49), (51) and (52). Substitution of Eqs. (51) and (52) into Eq. (49) yields a non-linear vector equation for the unknown vector $\mathbf{a}_{n+1}$. The Newton–Raphson method to determine $\mathbf{a}_{n+1}$ may be expressed as

$$\mathbf{a}^{(i+1)}_{n+1} = \mathbf{a}^{(i)}_{n+1} - \mathbf{J}^{-1}(\mathbf{a}^{(i)}_{n+1})\mathbf{R}(\mathbf{a}^{(i)}_{n+1}), \tag{55}$$

where i represents the iteration number at each time step, $\mathbf{J}(\mathbf{a}^{(i)}_{n+1})$ is the Jacobian matrix given by

$$\mathbf{J}^{-1}(\mathbf{a}^{(i)}_{n+1}) = (1-\alpha_m)\mathbf{M} + 2(1-\alpha_f)\gamma\Delta t\Omega_{n+1-\alpha_f}\mathbf{G} + (1-\alpha_f)\beta\Delta t^2[\mathbf{K} - \Omega^2_{n+1-\alpha_f}\mathbf{M}_\Phi + \dot{\Omega}_{n+1-\alpha_f}\mathbf{G}_\Phi + \mathbf{K}^{(i)}_T] \tag{56}$$

and $\mathbf{R}(\mathbf{a}^{(i)}_{n+1})$ is a vector expressed as

$$\mathbf{R}(\mathbf{a}^{(i)}_{n+1}) = \mathbf{M}\mathbf{a}^{(i)}_{n+1-\alpha_m} + 2\Omega_{n+1-\alpha_f}\mathbf{G}\mathbf{v}^{(i)}_{n+1-\alpha_f} + [\mathbf{K} - \Omega^2_{n+1-\alpha_f}\mathbf{M}_\Phi + \dot{\Omega}_{n+1-\alpha_f}\mathbf{G}_\Phi]\mathbf{d}^{(i)}_{n+1-\alpha_f} + \mathbf{P}(\mathbf{d}^{(i)}_{n+1-\alpha_f}) - \mathbf{F}_{n+1-\alpha_f}. \tag{57}$$

In Eq. (56), $\mathbf{K}^{(i)}_T$ is the tangent matrix of $\mathbf{P}(\mathbf{d}_{n+1-\alpha_f})$ at $\mathbf{d}_{n+1-\alpha_f} = \mathbf{d}^{(i)}_{n+1-\alpha_f}$.

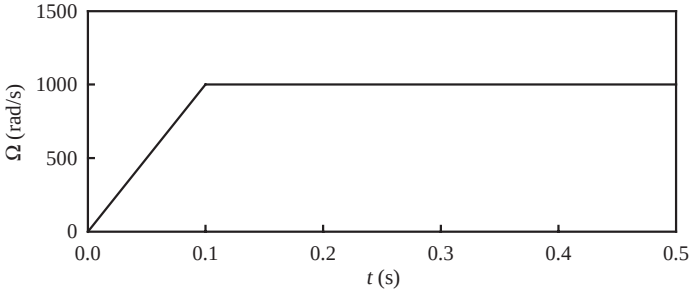

Fig. 10. Rotating speed profile of the disk with angular misalignment used to compute the time histories of the displacements.

Using the algorithm described in the above, the non-linear dynamic responses are computed for a rotating disk. The zero initial conditions of $\mathbf{d}_0 = \mathbf{v}_0 = \mathbf{0}$ are imposed and the unit impulsive pressure is applied to the disk in the z direction. The rotating speed and acceleration are described by the rotating speed profile shown in Fig. 10. The rotating speed increases from 0 to 1000 rad/s with the angular acceleration 10^4 rad/s^2 and then the speed remains constant. For time integration, the time step size is selected as $\Delta t = 10^{-4}$ s and the algorithmic parameters without numerical dissipation are used. The material properties and dimensions of the disk are the same as those of the previous section. All the responses are computed at a point on the outer periphery, which is defined by $r = b$ and $\theta = 45^\circ$.

The computed dynamic responses for the transverse displacement w are illustrated in Fig. 11. Fig. 11(a) is for the response when the angular misalignment is $\phi = 2^\circ$ while Fig. 11(b) is for the response when the misalignment is $\phi = 0^\circ$. Regardless of the amount of angular misalignment, it is shown in the time interval of 0–0.1 s that the transverse vibration periods and amplitudes decrease with the rotating speed. These behaviours are caused by the stiffening effect due to the centrifugal force. On the other hand, during the interval of the constant rotating speed, i.e., $0.1 \leqslant t \leqslant 0.5$, the response for $\phi = 2^\circ$ demonstrates the amplitude modulation which is not shown in the response for $\phi = 0^\circ$. This amplitude modulation is a contribution of the mode split discussed in the previous section. Another interesting phenomenon during $0.1 \leqslant t \leqslant 0.5$ is that the response for $\phi = 0^\circ$ oscillates about a zero value of the transverse displacement while the response for $\phi = 2^\circ$ oscillates about a non-zero value. The average values of w during $0.1 \leqslant t \leqslant 0.5$ are $w = 1.203$ and $w = 0$ mm for Figs. 11(a) and (b), respectively.

The radial and tangential displacements are plotted in Figs. 12 and 13. As shown in the time interval $0 \leqslant t \leqslant 0.1$ of Fig. 12, the radial displacements for both cases of $\phi = 2^\circ$ and $\phi = 0^\circ$ increase as the rotating speed increases. When the disk has the constant rotating speed, the amplitude modulation, which is not clearly visible in Fig. 12(a), exists even in the radial response of the disk with angular misalignment. If the response is magnified, the modulation can be clearly observed. Similar to the transverse and radial displacements, for the case of the tangential displacement of the disk with angular misalignment, the amplitude modulation is also exhibited, as shown in Fig. 13(a). If the disk is aligned perfectly, the radial and tangential displacements show no amplitude modulation as illustrated in Figs. 12(b) and 13(b). The reason why all the transverse, radial and tangential responses of the disk with angular misalignment exhibit the modulation is that the displacements are fully coupled to each other, as shown in Eqs. (18)–(20).

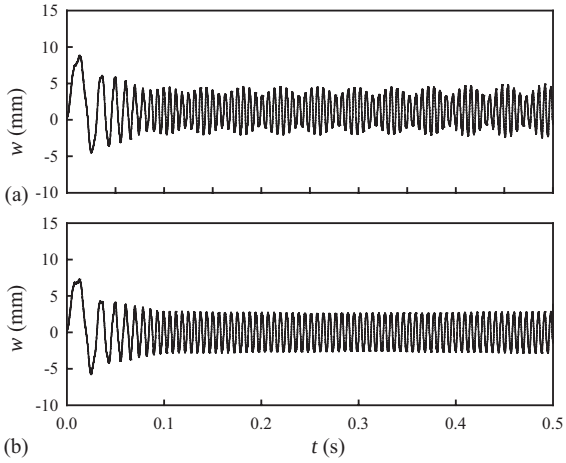

Fig. 11. Time histories of the transverse displacement w of the rotating disk: (a) when $\phi = 2^\circ$; and (b) when $\phi = 0^\circ$.

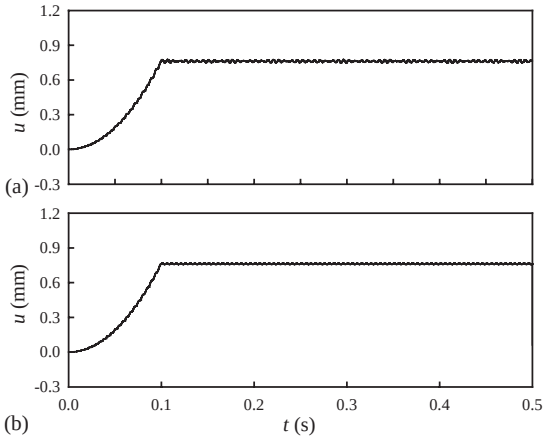

Fig. 12. Time histories of the radial displacement u of the rotating disk: (a) when $\phi = 2^\circ$; and (b) when $\phi = 0^\circ$.

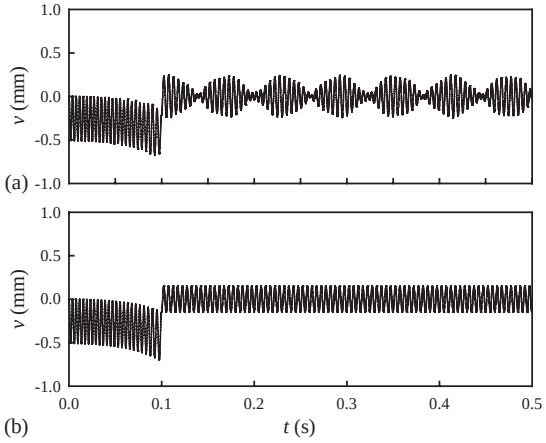

Fig. 13. Time histories of the tangential displacement v of the rotating disk: (a) when $\phi = 2^\circ$; and (b) when $\phi = 0^\circ$.

6. Summary and conclusions

The dynamic characteristics and responses are analyzed for the rotating disk with angular misalignment. The equations of motion for the disk are derived considering the rotating speed and acceleration. The derived equations are fully coupled equations between the transverse, radial and tangential displacements. The equation of transverse motion is a non-linear partial differential equation while the equations of radial and tangential motions are linear partial differential equations. After the equations of motion and the associated boundary conditions are transformed into the weak form, the non-linear matrix–vector equation is derived by using the finite element method. Based on the equation linearized around the equilibrium position, the effects of angular misalignment on the natural frequencies and mode shapes are analyzed. Furthermore, from the non-linear dynamic responses computed by the generalized-α method, the influence of angular misalignment on the dynamic responses is also investigated.

The results of the analysis for the natural frequencies and the mode shapes can be summarized as follows:

1. For all the out-of-plane modes with the nodal diameter, the natural frequency is split into two if the rotating disk has angular misalignment.
2. The amount of frequency split increases with the rotating speed as well as the angular misalignment.
3. The (0,1) out-of-plane mode exhibits the largest amount of frequency split compared to the other modes.
4. The asymmetric (0,1) and (0,2) out-of-plane modes rotate by approximately 90° and 45° from the symmetric (0,1) and (0,2) modes, respectively.
5. The frequency split in the in-plane mode is caused not by the angular misalignment but by the gyroscopic effect.

On the other hand, the analysis for the non-linear dynamic responses yields the following results:

1. When the rotating disk has angular misalignment, the transverse, radial and tangential dynamic responses demonstrate the amplitude modulation.
2. When the rotating speed is constant, the transverse response for the disk without angular misalignment oscillates about a zero displacement while the response for the disk with misalignment oscillates about a non-zero one.
3. Regardless of the amount of angular misalignment, the vibration periods and the vibration amplitudes decrease with the rotating speed.

Acknowledgements

The authors are grateful for the financial support provided by a grant (grant number: R01-2000-000-00292-0(2002)) from the Korea Science and Engineering Foundation (KOSEF).

References

[1] S.A. Tobias, R.N. Arnold, The influence of dynamical imperfection on the vibration of rotating discs, *Proceedings of the Institution of Mechanical Engineers* 171 (1957) 669–690.
[2] A.W. Leissa, P.A. Laura, R.H. Guiterez, Transverse vibrations of circular plates having nonuniform edge constraints, *Journal of the Acoustical Society of America* 66 (1979) 180–184.
[3] R.G. Parker, C.D. Mote, Exact perturbation for the vibration of almost annular or circular plates, *Journal of Vibration and Acoustics* 118 (1996) 436–445.
[4] R.G. Parker, C.D. Mote, Vibration and coupling phenomena in asymmetric disk–spindle systems, *American Society of Mechanical Engineers Journal of Applied Mechanics* 63 (1996) 953–961.
[5] J.G. Tseng, J.A. Wickert, On the vibration of bolted plate and flange assemblies, *American Society of Mechanical Engineers Journal of Vibration and Acoustics* 116 (1994) 468–473.
[6] J.G. Tseng, J.A. Wickert, Vibration of an eccentrically clamped annular plate, *American Society of Mechanical Engineers Journal of Vibration and Acoustics* 116 (1994) 155–160.
[7] A. Phylactopoulos, G.G. Adams, Transverse vibration of a rectangularly orthotropic rotating disk, Part 1: formulation and free vibration, *American Society of Mechanical Engineers Journal of Vibration and Acoustics* 121 (1999) 273–279.
[8] A. Phylactopoulos, G.G. Adams, Transverse vibration of a rectangularly orthotropic rotating disk, Part 2: forced vibration and critical speeds, *American Society of Mechanical Engineers Journal of Vibration and Acoustics* 121 (1999) 280–285.
[9] M. Kim, J. Moon, J.A. Wickert, Spatial modulation of repeated vibration modes in rotationally periodic structures, *American Society of Mechanical Engineers Journal of Vibration and Acoustics* 122 (2000) 62–68.
[10] J. Chung, J.W. Heo, C.S. Han, Natural frequencies of a flexible rotating disk misaligned with the axis of rotation, *Journal of Sound and Vibration* 260 (2003) 763–775.
[11] J.W. Heo, J. Chung, K. Choi, Dynamic time responses of a flexible rotating disk misaligned with the axis of rotation, *Journal of Sound and Vibration* 262 (2003) 25–44.
[12] J. Chung, G.M. Hulbert, A time integration algorithm for structural dynamics with improved numerical dissipation: the generalized-α method, *American Society of Mechanical Engineers Journal of Applied Mechanics* 60 (1993) 371–375.
[13] J. Chung, J.M. Lee, Vibration analysis of a nearly axisymmetric shell structure using a new finite ring element, *Journal of Sound and Vibration* 219 (1999) 35–50.